arXiv:0810.3950v1 [astro-ph] 22 Oct 2008

Study on X-ray Spectra of Obscured AGNs based on Monte Carlo simulation - an interpretation of observed wide-band spectra

Shinya Ikeda[1], Hisamitu Awaki[1], and Yuichi Terashima[1]

Department of Physics, Ehime University, Matsuyama, 790-8577, Japan

awaki@astro.phys.sci.ehime-u.ac.jp

ABSTRACT

Monte Carlo simulation is one of the best tools to study the complex spectra of Compton-thick AGNs and to figure out the relation between their nuclear structures and X-ray spectra. We have simulated X-ray spectra of Compton-thick AGNs obscured by an accretion torus whose structure is characterized by a half-opening angle, an inclination angle of the torus relative to the observer, and a column density along the equatorial plane. We divided the simulated spectra into three components: one direct component, an absorbed reflection component and an unabsorbed reflection component. We then deduced the dependencies of these components on the parameters describing the structure of the torus. Our simulation results were applied to fit the wide-band spectrum of the Seyfert 2 galaxy Mrk 3 obtained by *Suzaku*. The spectral analysis indicates that we observe the nucleus along a line of sight intercepting the torus near its edge, and the column density along the equatorial plane was estimated to be $\sim 10^{24}$ cm^{-2}. Using this model, we can estimate the luminosities of both the direct emission and the emission irradiating the surrounding matter. This is useful to find the time variability and time lag between the direct and reflected light.

Subject headings: galaxies: active — galaxies: Seyfert — radiative transfer — X-rays: individual (Mrk3)

1. Introduction

Active galactic nuclei (AGN) emit huge amounts of energy as a result of accretion of matter onto supermassive black holes (hereafter SMBHs). Strong hard X-ray emission from these nuclei can be represented by power-law emission with a canonical photon index of $\sim$1.9. The strong emission irradiates material around the SMBH, leading to reprocessing of the

emission. Observation of the reprocessed emission is conducive to revealing the environment of the black hole, and hence help to understand the problems of the fuel supply and evolution of SMBHs.

Compton-thick AGNs are suitable for the study of the reprocessed emission in AGNs, since their reprocessed emission dominates over the direct emission below 10 keV due to large column density $N_{\rm H} > 10^{24}$ cm^{-2}. In addition, Compton-thick AGNs are thought to be abundant in the local universe (e.g., Risaliti et al. 1999). Thus, these objects are important for understanding some key problems in AGN research, for example synthesis modeling of the Cosmic X-ray Background (e.g., Ueda et al. 2003) and the growth of AGNs. However, their spectra are so complex that the detailed nature of Compton-thick AGNs has thus far been unclear. There is another problem for spectral analyses of Compton-thick AGNs. The baseline model based on previous observations, which consists of both a direct and a reflection component, has been used to reproduce the complex X-ray spectra of Compton-thick AGNs (e.g., Magdziarz & Zdziarski 1995; Cappi et al. 1999). This model worked well for reproducing their spectra, and has contributed to our understanding of AGN. However, it is difficult to obtain information about the structure of the surrounding material from spectral fitting with this baseline model because the reflection model was developed for an accretion disc geometry. Thus, the reflection model does not match exactly with the actual reflection from the material around the black hole. Therefore we need a model that represents actual X-ray emission from the surrounding material using detailed Monte Carlo simulations.

Previous work that has investigated AGN X-ray spectra by means of Monte Carlo simulations so far includes the following. George & Fabian (1991) assumed a semi-infinite, plane-parallel configuration, and they calculated reflection from a plane-parallel slab. Wilman & Fabian (1999) computed transmission through a homogeneous sphere of cold material with a radius determined by its column density. Awaki et al. (1991) and Ghisellini et al. (1994) computed X-ray spectra emitted from AGNs and assumed a torus structure which has an open reflecting area characterized by its half-opening angle. However, these results were not applied to make available convenient spectral-fitting models to reproduce the X-ray spectrum of, for example, a Seyfert 2 galaxy.

We assume surrounding material with a 3D torus configuration and then simulate a spectrum from an AGN, considering the effect of Compton down-scattering and absorption. Performing Monte Carlo simulations, we investigate the relation between continuum emissions and the structure of the torus. Furthermore, the strength of iron line is important to reveal the existence of a hidden nucleus (e.g., Maiolino et al. 1998). Thus, we also investigate a dependency of the iron line on the structure of the torus. We apply our simulation

results to the spectral fitting of the X-ray spectrum of Mrk 3 observed with *Suzaku*, thereby constraining the structure of the torus in this Seyfert 2 galaxy.

2. Model Definition and Calculation

2.1. Basic Assumptions

In our Monte Carlo simulation, we adopted a standard spherical coordinate system with the radial distance (r) from the origin, the zenith angle (θ) from the Z-axis, and the azimuthal angle (ϕ) from the X-axis. A primary radiation source was placed at the origin, and illuminates the surrounding material. The material was assumed to be neutral and cold ($T \leq 10^6$ K).

We took into account photoelectric absorption, iron fluorescence, and Compton scattering in our simulation. The photoelectric absorption cross-section, $\sigma_{\rm abs}$, was calculated by using the NIST XCOM database [1] and the cosmic elemental abundances of Anders & Grevesse (1989). We also calculated the photoelectric absorption cross-section of Fe for deciding iron absorption events. Note that the cross-section by Balucinska-Church & McCammon (1992) is not valid for energies above 10 keV, and that the NIST cross-section in the 1–100 keV band is nearly equal to that by Verner et al. (1996) which is identified as *vern* in *XSPEC* (see Figure 1). The Compton scattering cross-section, $\sigma_{\rm es}$, was calculated with the Klein-Nishina formula. The number density of electrons, $n_{\rm es}$, for Compton scattering was related to the effective hydrogen number density, $n_{\rm H}$, by $n_{\rm es} = 1.2\ n_{\rm H}$.

We used the iron K-shell fluorescence yield of 0.34 (Bambynek et al. 1972) and a ratio 17:150 between the iron K_β and K_α fluorescence line transition probabilities (Kikoin 1976). Although the iron K_α fluorescence line consists of two components, $K_{\alpha1}$ and $K_{\alpha2}$ at 6.404 and 6.391 keV, respectively (for neutral iron) with a branching ratio of 2:1 (Bambynek et al. 1972), we made no distinction between $K_{\alpha1}$ and $K_{\alpha2}$ photons, adopting a common value of 6.40 keV. The iron K_β line is 7.06 keV for neutral iron.

2.2. Monte Carlo Simulation

A cross section view of the adopted structure of the torus is illustrated in Figure 2. The center of the torus is placed at the origin of the coordinate system, and the equatorial plane

[1] http://physics.nist.gov/PhysRefData/Xcom/Text/XCOM.html

of the torus structure lies in the X-Y plane. The structure of the torus is described by the following structure parameters: the half-opening angle $\theta_{\rm oa}$, the column density $N_{\rm H}$ along the equatorial plane, and inner ($r_{\rm in}$) and outer ($r_{\rm out}$) radii of the torus. We assumed $r_{\rm in}/r_{\rm out} = 0.01$ in our simulation. The angle $\theta_{\rm i}$ in Figure 2 presents the inclination angle of the torus relative to the observer.

A ray-trace method was adopted in our Monte Carlo simulation. The primary X-ray source was assumed to emit photons with the energy spectrum, $I(E) \propto E^{-0.9}\exp(-E/E_c)$, where E_c is a cut-off energy fixed at 360 keV. The spectrum is typical for Type 1 AGNs (e.g., Madau et al. 1994). The primary X-ray source was assumed to be isotropic. Each photon from the primary source had both an initial energy and an initial direction of propagation. In the case that a photon was injected into the torus, an interaction point of the photon was calculated by using a random number (see below). If the Compton scattering occurred at that point, the energy and the direction of photon was changed. The photon was tracked until it escaped the torus structure, or until it was absorbed in the torus. Note that when the photon with an energy above iron K-edge was absorbed by iron, a K-shell fluorescence line was isotropically emitted with a probability of the K-shell fluorescence yield in our simulation, where the iron absorption event was decided by using the ratio between the photoelectric absorption of iron and $\sigma_{\rm abs}$. Both energies and directions of propagation of all escaping photons were recorded in a photon list. For a given observed torus inclination angle of $\theta_{\rm i}$ (see Figure 2), we extracted photons whose zenith angles of propagation ranged within $\theta_{\rm i}\pm 1^{\circ}$, from the photon list, and then the extracted photons were accumulated into energy bins to form a spectrum.

The photon transportation in the torus is a key technique in our Monte Carlo simulation. The distance l to the next interaction is determined by the probability p, which is described as follows:

$$p = \exp(-\tau) = \int_0^l \exp(-\sigma_{\rm tot}\ n_{\rm H}) dl, \tag{1}$$

where τ and $\sigma_{\rm tot}$ are an optical depth and the total cross section of the interaction, respectively. The $\sigma_{\rm tot}$ is comprised of the sum of $\sigma_{\rm abs}$ and $\sigma_{\rm es}$. By inverting the cumulative probability function, l is expressed as

$$l = \frac{\tau}{n_{\rm H}\sigma_{\rm tot}} = -\frac{1}{n_{\rm H}\sigma_{\rm tot}} \times \ln(p). \tag{2}$$

The distance l is calculated from a uniform random number between 0 and 1 referred to as p.

Another key in our simulation is Compton scattering. The scattering angle, $\theta_{\rm scat}$ (relative to its direction of propagation), is calculated by the differential cross-section for Compton scattering. We assumed that the differential cross-section was proportional to $(1+\cos^2\theta_{\rm scat})$, as for the Thomson differential cross-section, since this approximation is efficient for analysis of the *Suzaku* data below a few hundreds keV (e.g., George & Fabian 1991). We note that this assumption over-estimates back-scattering relative to forward scattering at high energies. The effect of this approximation is seen in the reflection components, and depends on the geometry and $N_{\rm H}$ of the torus. In order to estimate the effect, we performed a simulation in the case of $\theta_{\rm oa}$=40°, $\theta_{\rm i}$=41°, and $N_{\rm H}$=10^{25} cm^{-2}, and found that the change of the reflection components due to this assumption was ∼10% at 100 keV.

The azimuthal angle of the scattering, $\phi_{\rm scat}$, was randomly selected in the region $0° \leq \phi_{\rm scat} < 360°$. The energy of the scattered photon was changed to be $E_{\rm in}/(1+\frac{E_{\rm in}}{mc^2}(1-\cos\theta_{\rm scat}))$, where m and $E_{\rm in}$ are electron mass and energy of the photon before Compton scattering, respectively (e.g., Rybicki & Lightman 1979).

3. Results

3.1. Simulation Results

Figure 3 is an example of a simulated AGN spectrum with $N_{\rm H} = 10^{24}$ cm^{-2}, $\theta_{\rm oa} = 40°$, and $\theta_{\rm i} = 45°$. We generated a total number of 2.5×10^8 photons. The same number of photons were generated for each run throughout this paper. We separated the simulated spectrum into direct and reflection components, where the direct component has no interaction with the surrounding material, while the reflection component consists of X-ray photons reflected in the surrounding material. Since an reflection component, which was modeled by *pexrav* in XSPEC, was required in the *Suzaku* spectrum of Mrk 3 by Awaki et al. (2008), we divided the simulated reflection component into two, which are referred to as the reflection components 1 and 2. The reflection component 2 consists of photons emitted from the inner wall of the torus without obscuration by the torus. The reflection component 1 consists of the rest of the reflected photons (see Figure 2). We have studied the parameter dependence of these three components based on the simulations with various $N_{\rm H}$, $\theta_{\rm oa}$, and $\theta_{\rm i}$.

3.2. Dependence of the Continuum Emission on the Structure Parameters

3.2.1. $N_{\rm H}$ Dependence

For studying the $N_{\rm H}$ dependence, we simulated spectra of the three components with $N_{\rm H}$ = $5{\times}10^{23}, 10^{24}, 2{\times}10^{24}, 3{\times}10^{24}, 5{\times}10^{24}$, and 10^{25} cm^{-2}, and the simulated components are shown in Figure 4. In these runs, we set $\theta_{\rm oa} = 40^\circ$ and $\theta_{\rm i} = 50^\circ$. All the three components, especially the direct component, show a dependence on $N_{\rm H}$. It is expected that the direct component is affected only by the column density ($N^{\rm ls}$) along our line of sight. We compared the simulated direct components with the cut-off power-law models, which were affected by both photoelectric absorption and Compton scattering (Figure 5). It is found that the models were in good agreement with the simulated direct components. Please note that the column density $N^{\rm ls}$ is a function of $\theta_{\rm i}$, $\theta_{\rm oa}$ and the ratio $r_{\rm in}/r_{\rm out}$ (=r). The ratio of $N^{\rm ls}$ to the $N_{\rm H}$ is described as

$$N^{\rm ls}/N_{\rm H} = \frac{r(\cos\theta_{\rm i} - \cos\theta_{\rm oa}) + \sin(\theta_{\rm i} - \theta_{\rm oa})}{(1-r)(r\cos\theta_{\rm i} + \sin(\theta_{\rm i} - \theta_{\rm oa})}. \quad (3)$$

In the case of r=0.01, $\theta_{\rm oa} = 40^\circ$, and $\theta_{\rm i} = 50^\circ$, for example, the value of $N^{\rm ls}/N_{\rm H}$ is deduced to be 0.97.

3.2.2. Dependence on the Half-opening Angle, $\theta_{\rm oa}$

Three components depended on the half-opening angle, $\theta_{\rm oa}$, but we discuss the $\theta_{\rm oa}$-dependence of only the reflection components 1 and 2, since the $\theta_{\rm oa}$-dependence of the direct component, which is affected by N^{ls}, has been described by equation 3.

The left panel in Figure 6 shows simulated spectra of the reflection component 1 for $\theta_{\rm oa}$ = $10^\circ - 70^\circ$ in steps of 10°. The values of $N_{\rm H}$ and $\theta_{\rm i}$ were fixed at 10^{24} cm^{-2} and 90° in these runs, respectively. The spectral shape of the reflection component 1 has a small dependence on $\theta_{\rm oa}$, and the total photon count in the reflection component 1 decreases with increasing $\theta_{\rm oa}$. We plot the total count in Figure 7. Since some photons emitted from the central source escape through the opening area of the torus, the intensity of the reflection component 1 is dependent upon $\theta_{\rm oa}$. We compared the total counts of this component with the covering fraction of the torus, $\cos\theta_{\rm oa}$. In the right panel in Figure 8, we plot the normalized total counts, which are divided by the total counts in the case of spherical distribution of the surrounding material. It is found that the $\theta_{\rm oa}$-dependence of the reflection component 1 can be roughly explained by the covering fraction of the surrounding material. For large $N_{\rm H}$

of 10^{25} cm^{-2}, the total counts do not follow this $\theta_{\rm oa}$-dependence as for low $N_{\rm H}$ due to the absorption of the reflection component by the torus itself.

The right panel in Figure 6 shows the $\theta_{\rm oa}$-dependence of the reflection component 2. In these runs, we set $\theta_{\rm i}$=$\theta_{\rm oa}$+1° in order to obtain a high intensity of the reflection component 2 under the condition that the nucleus is obscured by the torus. The total count of the reflection component 2 are shown in Figure 7. It is found that the reflection component 2 is to be zero at both $\theta_{\rm oa}$ =0 and 90°, and has a maximum intensity at $\theta_{\rm oa} \sim 30°$. The reflection component 2 is emitted from the visible inner wall of the torus. Thus, this component vanishes at $\theta_{\rm oa}$ =0 due to there being no inner wall. This component is also associated with the total number of photons injected into the torus from the central source, which is related to the solid angle of the torus. Therefore, the intensity of the reflection component 2 is associated with a combination of both apparent size of the visible inner wall of the torus and solid angle of the torus, i.e. $\cos\theta_{\rm oa}\cos(2\theta_{\rm oa}-\pi/2)$. The left panel in Figure 8 shows the total counts of the reflection component 2 in $N_{\rm H}$=10^{23}, 10^{24}, and 10^{25} cm^{-2}. For the case of $N_{\rm H}$=10^{25} cm^{-2}, the $\theta_{\rm oa}$-dependence is well reproduced by the combination described as $\cos\theta_{\rm oa}\cos(2\theta_{\rm oa}-\pi/2)$, since the reflection occurs mainly on the inner surface of the torus.

3.2.3. Dependence on the Inclination Angle $\theta_{\rm i}$

We show simulated spectra of the reflection components for $\theta_{\rm oa}$=10° with $\theta_{\rm i}$=11° to 71° in steps of 20° in Figure 9, and show the total counts at $\theta_{\rm oa}$=10° and 30° against $\theta_{\rm i}$ from 1° to 89° in steps of 2° in Figure 10. In these runs, $N_{\rm H}$ was fixed at 10^{24} cm^{-2}. The reflection component 1 has a weak $\theta_{\rm i}$-dependence (see Figure 9), and has a similar intensity in $\theta_{\rm i} > \theta_{\rm oa}$ +10° (Figure 10). The $\theta_{\rm i}$-dependence is consistent with the fact that the reflection component 1 depends on the covering factor of the surrounding material as mentioned in the previous subsection. The unified model of Seyfert galaxies predicts that $\theta_{\rm i}$ is larger than $\theta_{\rm oa}$ in Seyfert 2 galaxies. Thus, for most Seyfert 2 galaxies, the reflection component 1 should show a small $\theta_{\rm i}$-dependence, and this component should depend on mainly $\theta_{\rm oa}$ and $N_{\rm H}$ of the torus. In the case of $\theta_{\rm oa} < \theta_{\rm i} < \theta_{\rm oa}$+10°, the reflection component 1 should have a strong $\theta_{\rm i}$-dependence.

The reflection component 2 shows a strong $\theta_{\rm i}$-dependence (Figure 9), because the component is emitted from the visible inner wall, whose area is decreasing with increasing $\theta_{\rm i}$. If we observe the source edge-on, i.e.; $\theta_{\rm i}$ =90°, the area of the wall is apparently zero for the observer. On the other hand, if we observe the source face-on, i.e.; $\theta_{\rm i}$=0°, the projected area (i.e. the area projected onto the sky, perpendicular to the line of sight) is largest. The $\theta_{\rm i}$-dependence of the reflection component 2 is roughly explained only by that of the projected

area. Note that larger portion of the projected area, or the visible inner region, is obscured by the near side of the torus with increasing $\theta_{\rm i}$ in $\theta_{\rm i} > \theta_{\rm oa}$. The spectral shape of the reflection component 2 is also affected by $\theta_{\rm i}$ as shown in Figure 9. With increasing $\theta_{\rm i}$, the low-energy cut off becomes more pronounced. This is because only X-rays reflected from the visible inner region of the torus (see Figure 2) contribute to the reflection component 2, as defined. Some photons emitted from the central source enter the far side of the torus and Compton scattered. A part of the scattered photons are absorbed inside the torus before they ever reach the visible inner region. Since the length of the path of such photons increases with $\theta_{\rm i}$, more photons are absorbed before they reach the visible region. As a result, we can see a $\theta_{\rm i}$-dependence on the spectral shape.

3.2.4. Note on dependence on $r_{\rm in}/r_{\rm out}$

The ratio $r_{\rm in}/r_{\rm out}$ (=r) was fixed at 0.01 in our simulation. We briefly discuss the spectral dependence on this ratio. We simulated the reflection components with different values of the ratio, 0.001, 0.01, 0.1, and 1. In these runs, $N_{\rm H}$, $\theta_{\rm oa}$, and $\theta_{\rm i}$ were set to be 10^{24} cm^{-2}, 40°, and 41°, respectively. The reflection component 1 shows a very weak dependence on this ratio, since these simulations were carried out for the same $\theta_{\rm oa}$, and this component depends mainly on the covering fraction of the torus. On the other hand, the reflection component 2 below $\sim$ 4 keV depends on the ratio r (Figure 11). Reflections occur more frequently than absorption at the inner region of the torus. Thus, in the case of the small r, the closest region to the source is obscured by the torus, since we consider the case of Seyfert 2 galaxies, $\theta_{\rm i} > \theta_{\rm oa}$. This effect is also seen in the $\theta_{\rm i}$ dependence of the reflection component 2 (see Figure 9). This study indicates that it is difficult to produce a strong unabsorbed reflection-component in our simple torus geometry with a small r (=0.001).

3.3. X-ray luminosity absorbed by the torus

In our simulation, X-rays emitted from the central source were absorbed by the dusty torus. It is important to compare the absorbed X-ray luminosity with the infrared luminosity, since the infrared luminosity is a good indicator for the absorbing luminosity in the torus. We estimated the fraction of the absorbed luminosity with respect to the intrinsic source luminosity. The intrinsic luminosity of the central X-ray source was calculated from the assumed spectrum in section 2.2, and the absorbed X-ray luminosity was derived from the subtraction of an output luminosity from the intrinsic luminosity, where the output luminosity was deduced from a total energy of the escaping photons from the torus structure.

Figure 12 shows the absorbing fraction to the 1–100 keV intrinsic luminosity as a function of $\theta_{\rm oa}$ in $N_{\rm H}$=10^{22}, 10^{23}, 10^{24}, and 10^{25} cm^{-2}. The dependence of the absorbing fraction is roughly explained by cos $\theta_{\rm oa}$, which displays the covering fraction of the dusty torus. In the case of $N_{\rm H}$ = 1×10^{24} cm^{-2} and $\theta_{\rm oa}$=45°, the absorbing fraction of 0.37 is obtained, and the absorbed luminosity is estimated to be 1.1×10^{43} erg s^{-1} for the 1–100 keV intrinsic luminosity of 3×10^{43} erg s^{-1}, which corresponds to the 2–10 keV intrinsic luminosity of 1×10^{43} erg s^{-1}.

The infrared luminosity has a good correlation with the 2–10 keV luminosity. By using the relation between these luminosities by Mulchaey et al. (1994), the infrared luminosity for an AGN with the 2–10 keV X-ray luminosity of 1×10^{43} erg s^{-1} is estimated to be 10^{44} erg s^{-1}, which is about 10 times larger than the absorbed X-ray luminosity. The dust in the torus is heated by optical and UV photons as well as X-ray photons. Our study shows an estimation of the fraction of the absorbed X-ray luminosity to dust heating. We indicate that the absorbed luminosity depends on the geometry of the torus, $\theta_{\rm oa}$ in Figure 12. Lutz et al. (2004) pointed out that the scatter in the relation between mid-infrared and absorption corrected hard X-ray luminosities was about one order of magnitude, and that the scatter was likely caused by the geometry of the absorbing dust. The scatter seen in the relation may be explained by the $\theta_{\rm oa}$-dependence of the absorbed luminosity.

3.4. Dependence of the Iron-line Emission on the Structure Parameters

A prominent iron line with an equivalent width of > a few 100 eV is an important characteristic of Seyfert 2 galaxies. The dependence of the equivalent width of the iron line on the structure parameters of the torus have been studied in previous work (e.g., Awaki et al. 1991; Ghisellini et al. 1994; Levenson et al. 2002). These studies were mainly performed for the equivalent width relative to the total continuum emission, comprised of the sum of the direct and reflection components. In our study, we have investigated the equivalent width relative to the reflection component (hereafter $EW_{\rm ref}$) as well as the equivalent width to the total continuum emission (hereafter $EW_{\rm tot}$). In Figures 13 and 14, we plot the equivalent width as a function of $N_{\rm H}$ and $\theta_{\rm oa}$ respectively (note that for $\theta_{\rm oa}$=0 we use a spherical distribution instead of using our simple torus model with $\theta_{\rm oa}$=0).

The left panel in Figure 13 shows the $N_{\rm H}$-dependence of $EW_{\rm tot}$ fixed at $\theta_{\rm oa}$=30°. We found that the $N_{\rm H}$-dependence is similar to those of previous studies, although our results are about 1.7 times larger than those obtained by Ghisellini et al. (1994). The difference may be caused by the difference of iron abundance used in the simulations. The right panel in Figure 13 shows the $\theta_{\rm oa}$-dependence of $EW_{\rm tot}$. The $EW_{\rm tot}$ in the Compton-thin region

($N_{\rm H} < 10^{24}$ cm^{-2}) decreases with increasing $\theta_{\rm oa}$. This $\theta_{\rm oa}$-dependence is represented by a function of $\cos\theta_{\rm oa}$, similar to the reflection component 1, since the iron line intensity is proportional to the solid angle subtended by the surrounding matter at the source.

The left panel in Figure 14 shows the $N_{\rm H}$-dependence of $EW_{\rm ref}$ for θ_{oa}=30°. The $EW_{\rm ref}$ shows little $N_{\rm H}$ dependence in the $N_{\rm H}$ <10^{24} cm^{-2}, since the $EW_{\rm ref}$ is mainly determined by the ratio between the absorption and scattering cross-sections. In the Compton-thick region, the $EW_{\rm ref}$ shows large $\theta_{\rm oa}$- and $\theta_{\rm i}$-dependences. This is caused by the fact that the contribution of the reflection component 1 to the reflection continuum at the iron band is decreasing with increasing $N_{\rm H}$ (see Figure 4).

We noted that the $EW_{\rm ref}$ in the Compton-thick regime is greater than 1000 eV in our simulations. Thus, observed lower values of $EW_{\rm ref}$, less than 1000 eV, may indicate a low metal abundance of iron.

4. Application to Observed Spectrum

By means of Monte Carlo simulations, we showed that the three continuum components depend on the structure parameters of the torus, $N_{\rm H}$, $\theta_{\rm oa}$, and $\theta_{\rm i}$. Our study suggests that we can estimate the structure of the torus by determining the three components in an observed spectrum. We therefore made a new model for spectral fitting based on our simulations with $1\times$ 10^9 photons in each run. In our new model, the direct component is reproduced by $phabs*compcabs*(cutoffpl)$ in $XSPEC$, where *compcabs* is a new model that we made for representing Compton scattering, and the two reflection components are reproduced by using table models, which have parameters of photon index, $N_{\rm H}$, $\theta_{\rm oa}$, and $\theta_{\rm i}$, since the reflection components are too complex to be represented by numerical expression. The table models cover the ranges of photon index of $1.5-2.5$, $N_{\rm H}$ of $10^{22}-10^{25}$ cm^{-2}, $\theta_{\rm oa}$ of $0°-70°$, and $\theta_{\rm i}$ of $0-90°$. The details of the parameters of the table models are listed in Table 1.

The Suzaku satellite can obtain a wide-band spectrum with good quality (Mitsuda et al. 2007). We applied the new model to the wide-band spectrum of Mrk 3 observed by the Suzaku satellite on 2005 October 22-23 during the SWG phase. We obtained XIS and HXD spectra in the same manner as described by Awaki et al. (2008), and then simultaneously fitted the XIS and HXD spectra above 1 keV with the new model defined as follows:

$$I(\text{ph s}^{-1}\text{ cm}^{-2}\text{ keV}^{-1}) = PL1+e^{-\sigma_{\rm a}N_{\rm H1}}e^{-\sigma_{\rm es}N_{\rm H1}}PL2+reflection1(N_{\rm EL})+reflection2(N_{\rm H2})+ELs, \quad (4)$$

where PL1 and PL2 are power law components with a high energy cut-off. The high energy cutoffs of both PL1 and PL2 were fixed at 360 keV, which is consistent with the cut-off energy

(E_{cut}) of the power law component $E_{cut} > 200$ keV obtained by Cappi et al. (1999). $N_{\rm H1}$ is the column density along our line of sight. We used the absorption cross-section of *vern* for $\sigma_{\rm a}$ in the *phabs* model in $XSPEC$ v12.4. The abundances of Anders & Grevesse (1989) were used. The $\sigma_{\rm es}$ is a Compton scattering cross-section, which is used in the *compcabs* model. The reflection components 1 and 2 in our simulation were reproduced by the two table models, $reflection1$ and $reflection2$, respectively. We set their photon indices equal to that of PL2, while we did not link their nomalizations to that of PL2, and their column densities along the equatorial plane ($N_{\rm H2}$) were not linked to the column density ($N_{\rm H1}$) of PL2 in our spectral fit. The emission lines (ELs) seen in the spectrum were represent by the sum of Gaussian components:

$$ELs = \sum_{\rm i} gauss(E_{\rm i}, \sigma_{\rm i}, N_{\rm i}), \tag{5}$$

where $E_{\rm i}$, $\sigma_{\rm i}$, and $N_{\rm i}$ are the center energy, width, and intensity of the i-th line. We fixed $E_{\rm i}$ and σ_i at the values obtained by Awaki et al. (2008).

We fitted the spectra with the new table models in the energy range from 1 to 70 keV. Since the table models were generated from simulations, the table models have statistical deviations. A typical standard deviation per 20 eV bin of the sum of $reflection$ 1 and 2 in the 3–5 keV band is about 2%, which is about 1/5 of the statistical error of the observed data in this energy band. Due to the deviations of the table models, the χ^2 will have a fluctuation of about (bin number)$\times(\frac{1}{5})^2$, which is estimated to be about 5. Thus, it is hard to find the best-fit parameters and their confidence regions with the χ^2-fitting procedure. We performed χ^2-test with our table models on the parameter grids of $\theta_{\rm oa}$ and $\theta_{\rm i}$ in order to examine whether we can obtain the structure parameters from the spectral fit with the table models. Table 2 lists the χ^2 on the grids with 612 d.o.f. The minimum χ^2 ($\chi^2_{\rm min}$) was obtained for $\theta_{\rm i} < \theta_{\rm oa}$, and the χ^2 was more than $\chi^2_{\rm min}$ + 30 for $\theta_{\rm i} > \theta_{\rm oa}$+3°. Since the $\theta_{\rm i}$ must be larger than the $\theta_{\rm oa}$ in our simple torus model (otherwise the $N_{\rm H1}$ becomes zero), the χ^2 study indicates that we observed the Mrk 3 nucleus near the edge of the torus. This is expected from the strong unabsorbed reflection component of Mrk 3 in the baseline model.

On the other hand, we found that it is difficult to constrain the half-opening angle $\theta_{\rm oa}$ from the spectral analysis, since the shapes of the reflection components 1 and 2 show a little $\theta_{\rm oa}$-dependence (Figure 6). Although their intensities depend on $\theta_{\rm oa}$ as shown in Figure 7, the intensities of the reflection components also depend on the luminosity of the central source. Figure 15 shows the change of the normalization of the direct and reflection components for $\theta_{\rm i}$=$\theta_{\rm oa}$+1°. The normalization of the reflection component is roughly proportional $1/\cos\theta_{\rm oa}$. This relation indicates that the contribution of the reflection components to the observed spectrum is nearly constant. Furthermore, the spectral shape of the reflection component

1 in the 5–70 keV band is similar to that of the direct component at $N_{\rm H}$ $\sim$$10^{24}$ cm^{-2} (see Figure 3). As a result, it is hard to constrain $\theta_{\rm oa}$, even if we link the intensities between the direct and reflection components. We note that the iron EW is not helpful to find the $\theta_{\rm oa}$ of Mrk 3, since $EW_{\rm ref}$ has a little dependence on $\theta_{\rm oa}$ in $N_{\rm H} < 10^{24}$ cm^{-2}.

In order to constrain $N_{\rm H2}$, we fitted the observed spectrum with our model on the grid of $N_{\rm H2}$. Since we did not constrain the $\theta_{\rm oa}$ from the spectral fit, we fixed $\theta_{\rm oa}$ at 50°, and θ_i at $\theta_{\rm oa}$+1°. The value of $N_{\rm H1}$ was a free parameter in this fit. We found that there is a χ^2 minimum around $\sim$$10^{24}$ cm^{-2}, and that the χ^2 is greater than $\chi^2_{\rm min}$+30 for $N_{\rm H2} < 6\times10^{23}$ and for $N_{\rm H2} > 2\times10^{24}$ cm^{-2}. We found that we constrain the structure parameter $N_{\rm H}$ of the torus by using our new model.

The opening angle may be estimated from the opening angle of the NLR. Capetti et al. (1995) found a NLR opening angle in Mrk 3 of $> 100°$. The half opening angle of $>50°$ is larger than the estimation by Ruiz et al. (2001) due to the inclusion of all the Z-shape emission components in the NLR in the estimation of Capetti et al. (1995). We here set θ_{oa} = 50° and $\theta_{\rm i} = 51°$ in our spectral fit. Furthermore, the column density $N_{\rm H1}$ was linked with $N_{\rm H2}$ by $N_{\rm H1}$=0.74 $N_{\rm H2}$, by using the equation (3). We obtained a small reduced χ^2 value of 1.18 (d.o.f.=613), which is comparable to that with the baseline model. Table 3 shows the best-fit parameters, and Figure 16 shows the best-fit spectrum. The photon index of the power law component and the column density of $N_{\rm H1}$ were estimated to be $\sim$1.82 and $\sim$$1.1\times10^{24}$ cm^{-2}, respectively. The intrinsic luminosity of the power law component in the 2–10 keV band was estimated to be 2.1×10^{43} erg s^{-1}, which is about 1.3 times that of the estimate with the baseline model and is consistent with that obtained by using the model with *plcabs* (Awaki et al. 2008), which describes the X-ray transmission, correctly taking into account Compton scattering (Yaqoob 1997). On the other hand, the intrinsic luminosity irradiating the accretion torus is estimated to be 5.1×10^{43} erg s^{-1} from the normalization of the reflection component. The discrepancy of the intrinsic luminosities between the direct and reflection components may be arisen by a time lag of the reflection component, since the long time variability of Mrk 3 has been reported and the distance of the accretion torus is estimated to be greater than 1 pc from the center (e.g., Awaki et al. 2000, 2008).

5. Summary and Conclusion

We simulated AGN spectra by using the ray-trace method, and made a new model for fitting spectra of Compton-thick AGNs. In our simulations we assumed an accretion torus surrounding a nucleus, which was characterized by $\theta_{\rm oa}$, $\theta_{\rm i}$, $N_{\rm H}$, and the ratio of the inner and outer radii of the torus. We considered interactions of photoelectric absorption,

iron fluorescence, and Compton scattering in the simulation. The simulated spectra were separated into three components: one direct component and two reflection components.

The direct component consists of X-ray photons which have no interaction with the surrounding material, and the component is only affected by column density along our line of sight. In fact, the direct component was well modeled with a cut-off power law emission affected by both photoelectric absorption and Compton scattering. On the other hand, the reflection components had not only an $N_{\rm H}$-dependence but also both $\theta_{\rm oa}$- and $\theta_{\rm i}$-dependences. The reflection component 1 shows a $\theta_{\rm oa}$-dependence, which is explained by the covering factor of the torus. The reflection component 2 has dependence on both $\theta_{\rm oa}$ and $\theta_{\rm i}$. The dependence of the reflection component 2 is roughly explained by the apparent size of the visible inner wall of the torus.

We fitted the *Suzaku* Mrk 3 spectrum with the new model based on our simulations, and found that the spectrum could be represented by our model. The structure parameters of the torus of Mrk 3 were estimated with the new model: $\theta_{\rm i} \sim \theta_{\rm oa} + 1^\circ$ and $N_{\rm H} \sim 10^{24}$ cm^{-2}, although it was hard to constrain $\theta_{\rm oa}$ from our spectral analysis. We estimated the intrinsic luminosity of the direct component and the intrinsic luminosity irradiating the surrounding matter. Assuming $\theta_{\rm oa}$=50° and $N_{\rm H1}$=0.76$N_{\rm H2}$, the 2–10 keV luminosity of the direct component was estimated to be about 2/5 of that irradiating the surrounding matter. This may be explained by time variability of Mrk 3 and time lag between the direct and reflected lights.

We demonstrated that we can bring out the structure of the torus from an observed X-ray spectrum with our new model. The wide-band X-ray spectra will be helpful to determine the structure of AGNs.

We also thank Drs. T. Yaqoob and K. Murphy for useful discussions and careful reading. We also thank the anonymous referee for helpful comments and suggestions. This study is carried out in part by the Grant support for Scientific Research of Ehime university (H.A.) and the Grant-in-Aid for Scientific Research (17740124 Y.T.) of the Ministry of Education, Culture, Sports, Science and Technology.

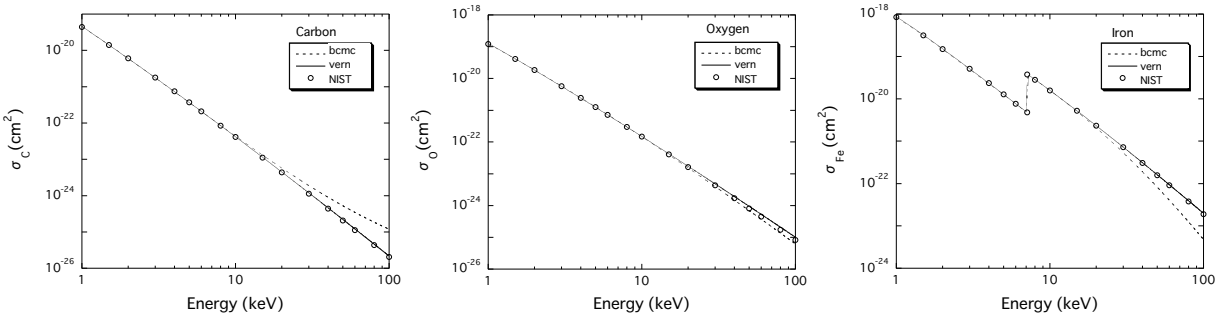

Fig. 1.— Photoabsorption cross-section of Carbon, Oxygen, and Iron. The open circles indicate those obtained from the NIST database. The solid and dashed lines show those by Verner et al. (1996) and Balucinska-Church & McCammon (1992), respectively. Their cross-sections are referred to as *vern* and *bcmc* in $XSPEC$.

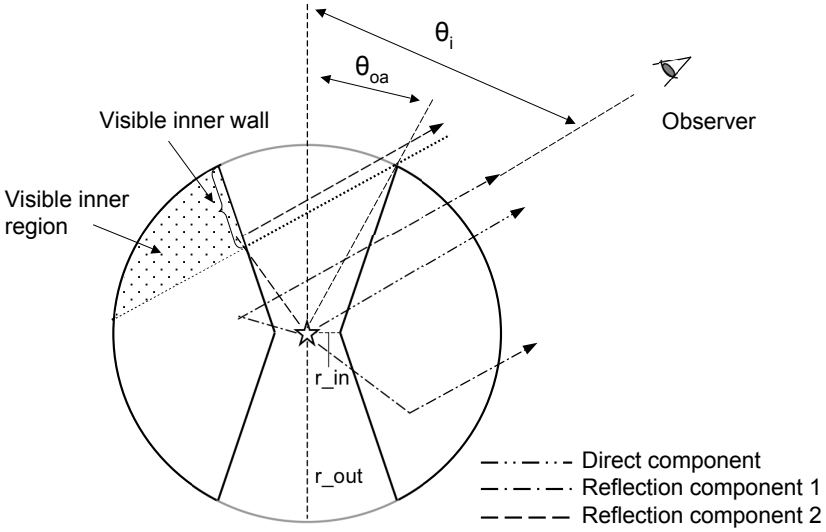

Fig. 2.— A cross section view of the torus structure in our simulation. The primary X-ray source is located at the center of an obscuring torus. The torus structure is characterized by the half-opening angle $\theta_{\rm oa}$, the inclination angle of the torus from an observer $\theta_{\rm i}$, the column density $N_{\rm H}$ along the equatorial plane, and the ratio of $r_{\rm in}$ to $r_{\rm out}$. A simulated spectrum is separated into three components: one direct component and two reflection components. The two reflection components are referred as reflection component 1 and 2. The reflection component 2 consists of reflection light from the visible inner wall of the torus. The reflection component 1 consists of the rest of the reflection light.

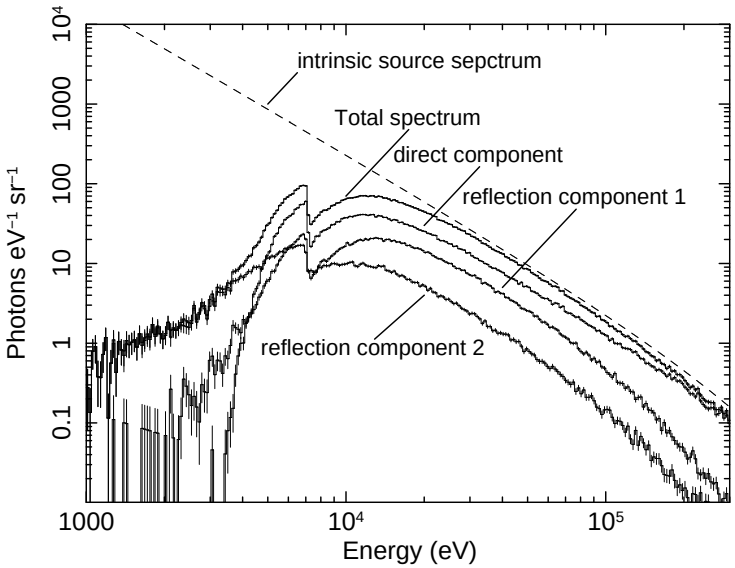

Fig. 3.— An example of our simulated AGN spectrum with $N_{\rm H} = 10^{24}$ cm^{-2}, $\theta_{\rm oa} = 40°$, and $\theta_{\rm i} = 45°$. The simulated spectrum is divided into three components : the direct component, the reflection component 1, and the reflection component 2 as shown in this figure. The dashed line displays the intrinsic source spectrum.

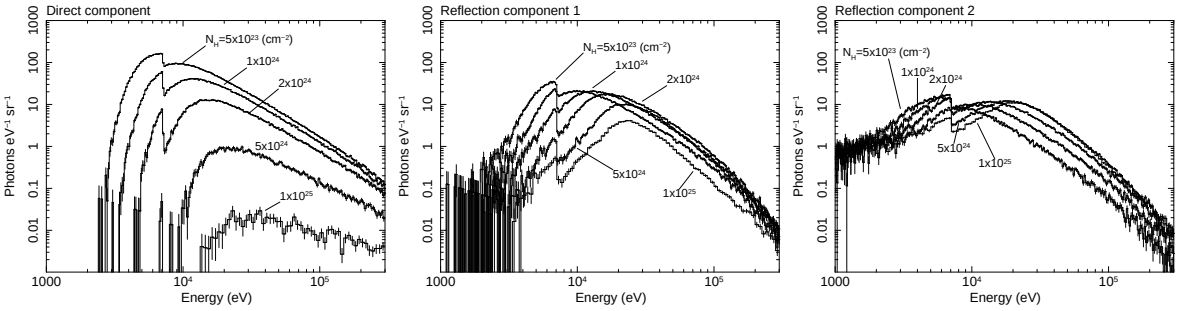

Fig. 4.— $N_{\rm H}$ dependence of the three components for $\theta_{\rm oa} = 40°$ and $\theta_{\rm i} = 45°$. The column density has values of $N_{\rm H} = 5{\times}10^{23},\ 10^{24},\ 2{\times}10^{24},\ 5{\times}10^{24}$ and 10^{25} cm^{-2}.

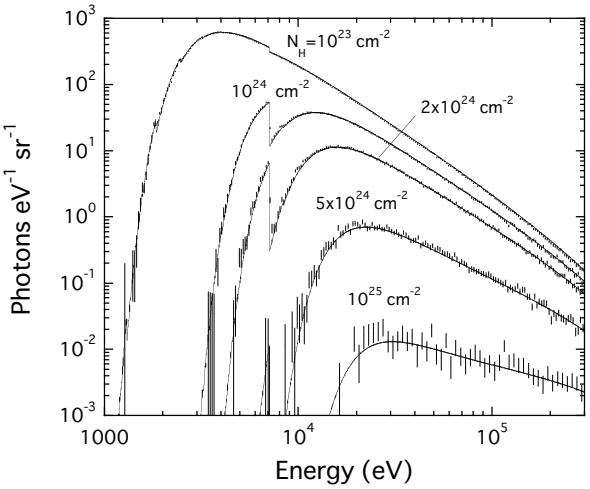

Fig. 5.— Comparison between the simulated direct component and the cut-off power law model affected by both photoelectric absorption and Compton scattering.

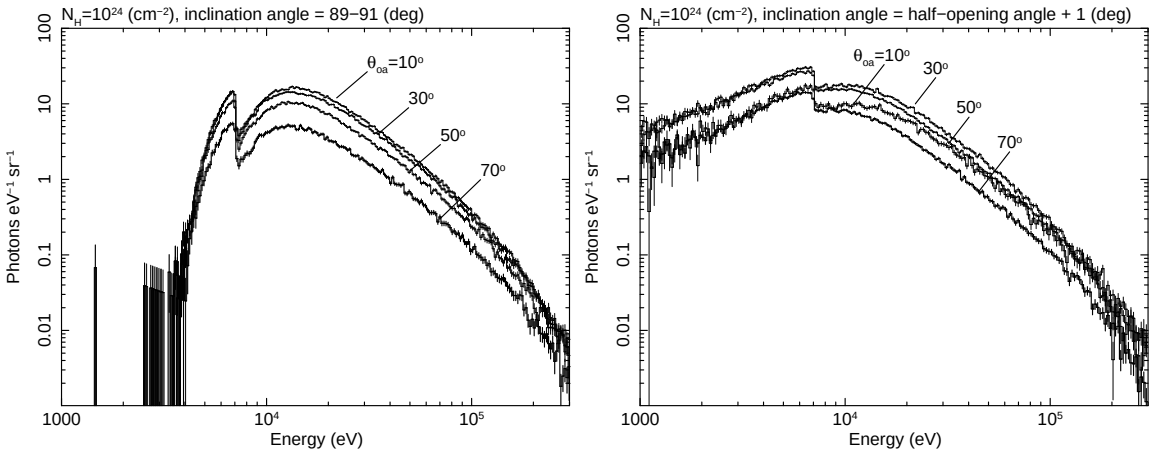

Fig. 6.— θ_{oa}-dependence of the reflection components 1 and 2. For the simulations of the reflection component 1, $N_{\rm H}$ and $\theta_{\rm i}$ were fixed at 10^{24} cm^{-2}, and 90°, respectively. For the simulations of the reflection component 2, $\theta_{\rm i}$ was fixed on $\theta_{\rm oa}$+1°.

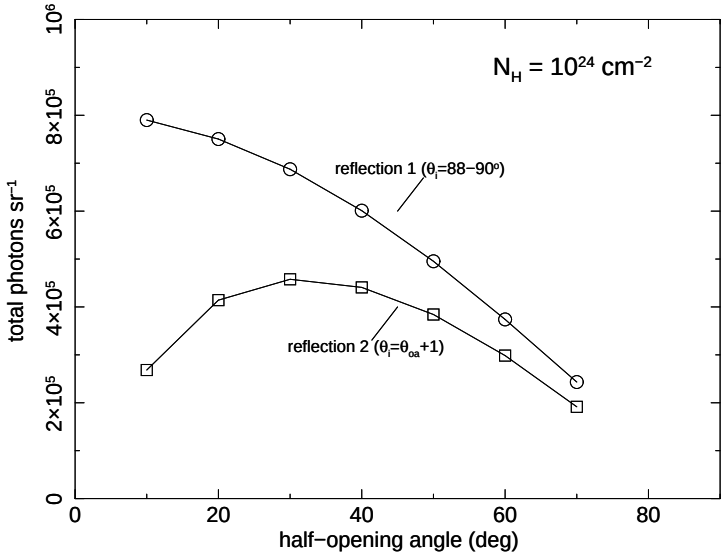

Fig. 7.— Total counts of the reflection components 1 and 2 as a function of $\theta_{\rm oa}$. Open circles and open squares represent the reflection component 1, and the reflection component 2, respectively.

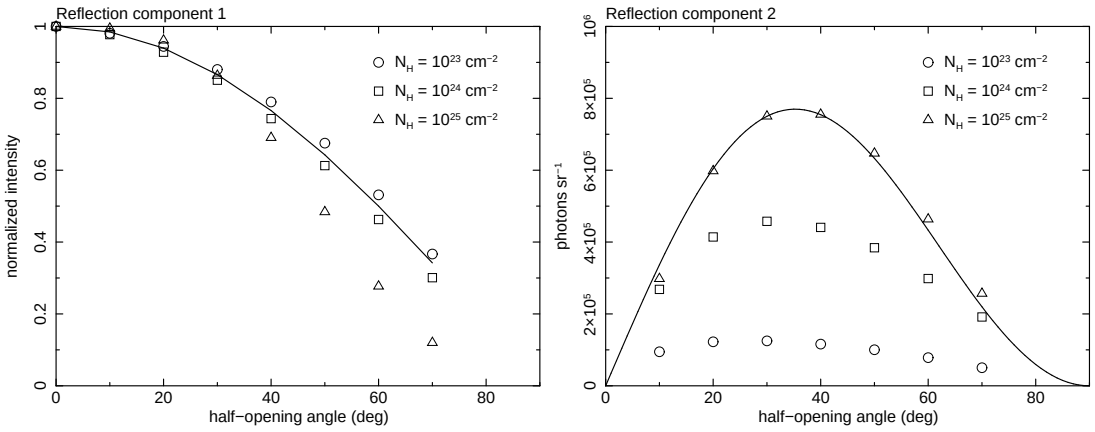

Fig. 8.— The θ_{oa} dependence of the reflection component 1 (left) and 2 (right) for various column densities, $N_{\rm H}$=10^{23}, 10^{24}, and 10^{25} cm^{-2}. The left panel shows the normalized count rate divided by that simulated in the spherical distributed matter. The solid lines in the left and right panels show the covering factor of the torus, $\cos\theta_{\rm oa}$, and the combination of the covering factor and the apparent size of the visible inner wall, $\cos\theta_{\rm oa}\,\cos(2\theta_{\rm oa}-\pi/2)$.

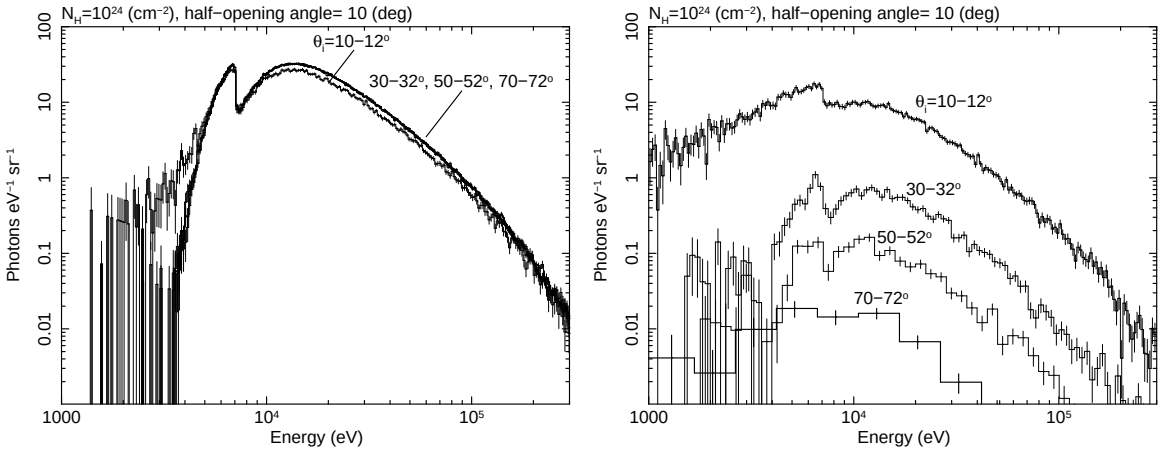

Fig. 9.— The $\theta_{\rm i}$-dependence of the reflection components 1 (left) and 2 (right). In these simulations, $N_{\rm H}$ and $\theta_{\rm oa}$ were set at 10^{24} cm^{-2} and 10°, respectively.

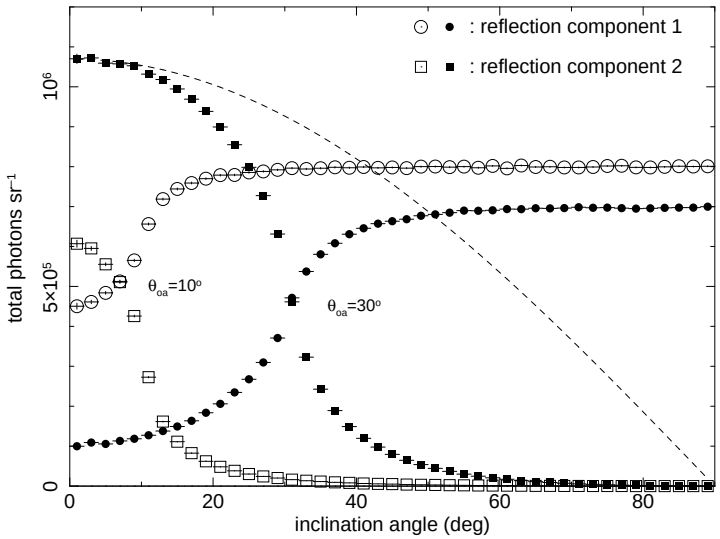

Fig. 10.— Total counts of the reflection components 1 and 2 in the 1 keV–300 keV band as a function of $\theta_{\rm i}$. Open circles and squares show the total counts of the reflection component 1 and 2 at $\theta_{\rm oa}$=10°, respectively. We also show the total counts for $\theta_{\rm oa}$= 30° by closed circles and squares. A curve of cos $\theta_{\rm i}$ is plotted in the dotted line, in order to show a $\theta_{\rm i}$-dependence of the projected area.

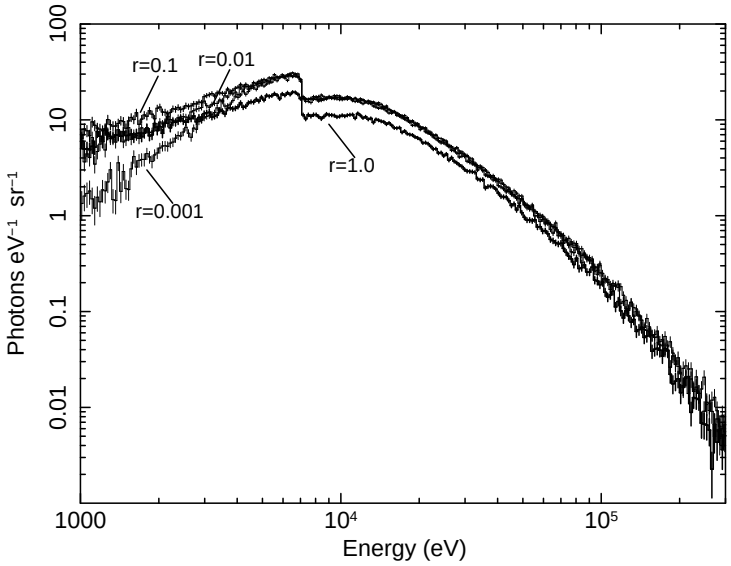

Fig. 11.— Simulated spectra of the reflection component 2 for different values of the ratio $r = r_{\rm in}/r_{\rm out}$.

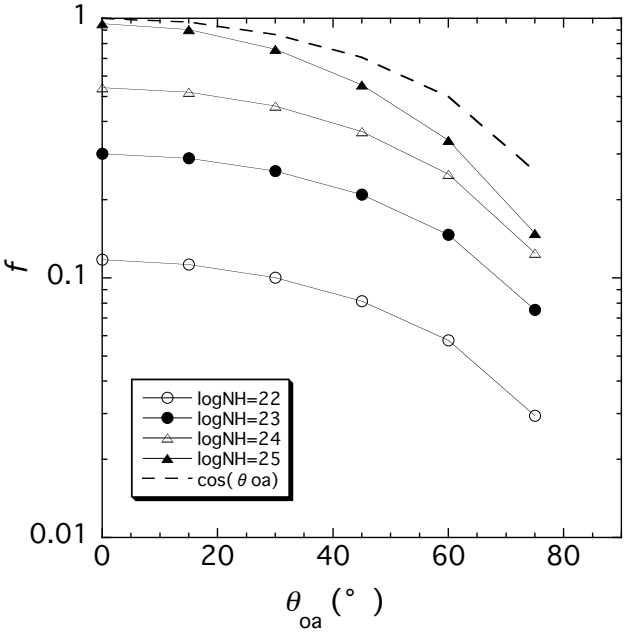

Fig. 12.— The fraction of the absorbed luminosity with respect to the intrinsic source luminosity. The fraction was estimated for $N_{\rm H}$=10^{22}, 10^{23}, 10^{24}, and 10^{25} cm^{-2}. We also plot a curve of cos $\theta_{\rm oa}$ in the dashed line, in order to display the covering factor of the dusty torus.

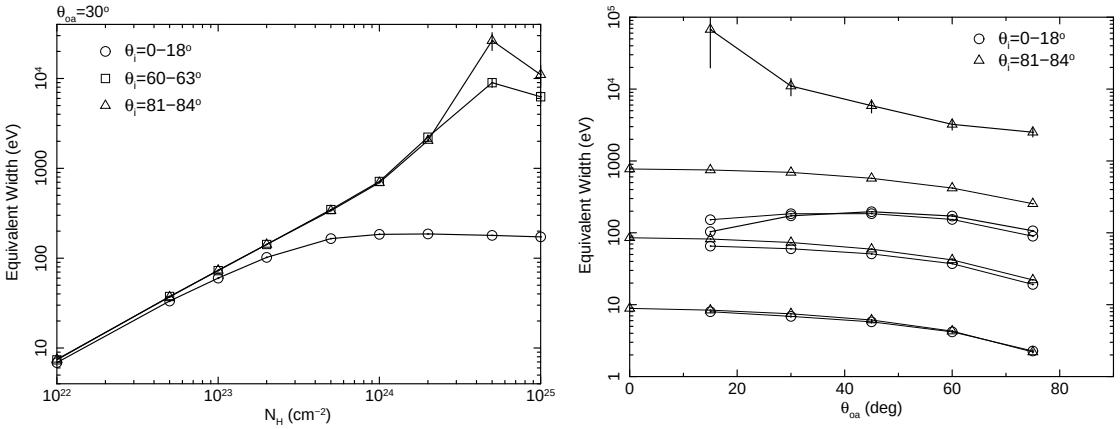

Fig. 13.— Equivalent width of the iron Kα line to the total continuum emission, summed over the direct and reflection components. The left panel shows the $N_{\rm H}$ dependence of the equivalent width for $\theta_{\rm oa}$=30°, and the right panel shows the dependence on $\theta_{\rm oa}$ for $N_{\rm H}$=10^{22}, 10^{23}, 10^{24}, and 10^{25} cm^{-2} from the bottom to the top (or from thin to thick lines). The open circles, squares, and triangles indicate the equivalent width in the ranges $\theta_{\rm i}$=0–18°, 60–63°, and 81–84°, respectively. We plot the equivalent width for the spherical distribution at $\theta_{\rm oa}$=0, instead of using our simple torus model with $\theta_{\rm oa}$=0.

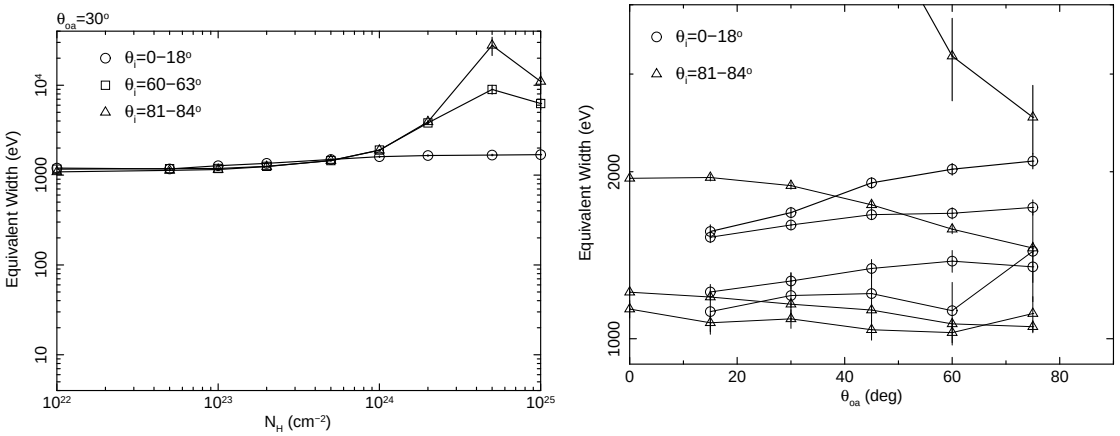

Fig. 14.— Equivalent width of the iron Kα line to the reflection components 1+2. Symbols are the same as in Figure 12.

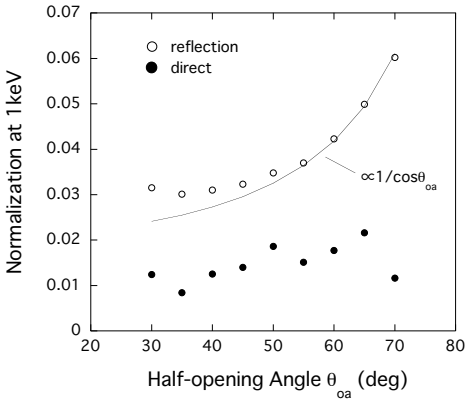

Fig. 15.— The normalization of the direct and reflection components as a function of $\theta_{\rm oa}$. $\theta_{\rm i}$=$\theta_{\rm oa}$+1° is assumed. The closed and open circles display their normalizations as shown in the figure. The solid line indicates a curve proportional to $1/\cos\theta_{\rm oa}$.

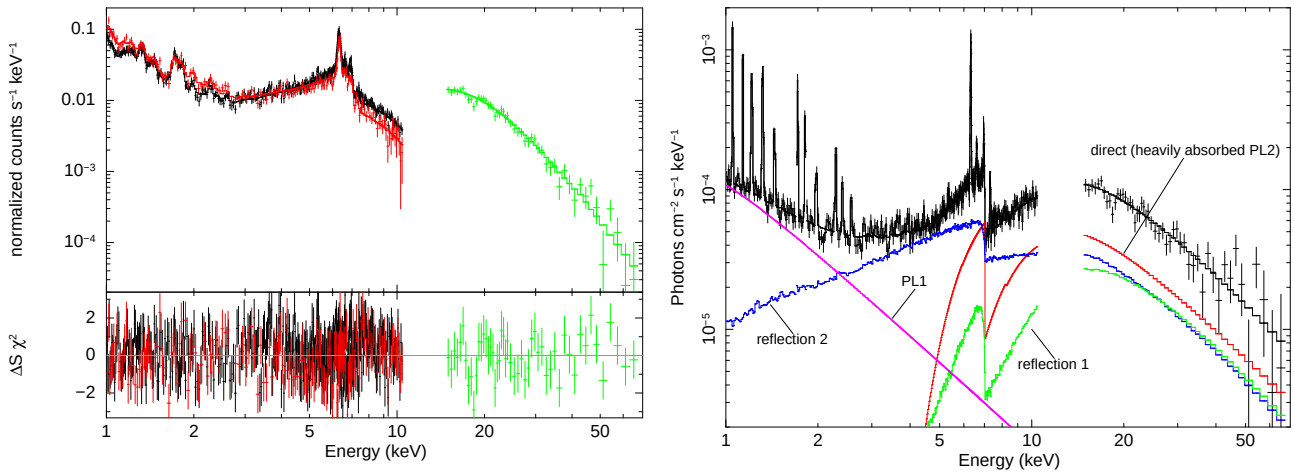

Fig. 16.— The wide-band spectrum of Mrk 3 observed with Suzaku fitted with our model (left), and the unfolded X-ray spectrum (right). The spectra in the left panel are obtained by the XIS-FI (black), XIS-BI (red), and HXD-PIN (green). The energy range around the Si-K edge (1.875-1.845 keV) is ignored for spectral fitting. The right panel shows continuum emission from PL1, reflection 1, reflection 2 and heavily absorbed PL2.

Table 1: Parameters and grids of table model

Parameters	Parameter grids
Photon index	1.5, 1.9, 2.5
$N_{\rm H}$ ($\times 10^{22}$ cm^{-2})	1, 5, 10, 50, 100, 200, 300, 500, 700, 1000
half-opening angle (°)	0, 10, 20, 30, 40, 50, 60, 70
inclination angle (°)[a]	1– 89 in steps of 2

[a]We selected X-rays within the inclination angle± 1°.

Table 2: χ^2 on the parameter grid of $\theta_{\rm oa}$ and $\theta_{\rm i}$.

$\theta_i - \theta_{\rm oa}$	$\theta_{\rm oa}$								
	30°	35°	40°	45°	50°	55°	60°	65°	70°
-2	704.6	706.7	706.2	702.1	701.9	700.8	706.6	703.3	706.3
-1	701.6	705.9	705.7	702.8	700.2	703.2	708.9	704.0	706.2
0	701.7	705.3	706.2	704.1	702.9	707.3	707.0	706.7	707.6
+1	705.1	710.2	711.5	708.8	711.8	710.2	713.4	713.6	723.6
+2	724.9	736.4	724.4	734.1	729.3	737.6	737.7	752.0	753.6

Table 3: Best-fit model parameters.

Photon Index	$N_{\rm H1}$ ($\times 10^{24}$ cm^{-2})	$L_{2-10}^{\rm direct}$ (erg s^{-1})	$N_{\rm H2}$ ($\times 10^{24}$ cm^{-2})	$L_{2-10}^{\rm refl}$ (erg s^{-1})	$\theta_{\rm oa}$ (°)	$\theta_{\rm i}$ (°)	χ^2/(d.o.f.)
1.82	1.1	2.1×10^{43}	1.5	5.1×10^{43}	50(fixed)	51(fixed)	726/613

Note. — $N_{\rm H1}$ was linked to $N_{\rm H2}$.

REFERENCES

Anders, E., & Grevesse, N. 1989, Geochim. Cosmochim. Acta, 197, 214

Awaki, H., Koyama, K., Inoue, H., & Halpern, J. P. 1991, PASJ, 43, 195

Awaki, H., Koyama, K., Inoue, H., & Halpern, J. P. 2000, ApJ, 43, 195

Awaki, H. et al. 2008, PASJ, 60, S293

Balucinska-Church, M., & McCammon, D. 1992, ApJ, 400, 699

Bambynek, W., Crasemann, B., Fink, R. W., Freund, H.-U., Mark, H., Swift, C. D., Price, R. E., & Rao, P. V. 1972, *Rev.Mod.Phys.*, 44, 716

Capetti, A., Macchetto, F., Axon, D.J., Sparks, W.B., & Boksenberg, A. 1995, ApJ, 448, 600

Cappi, M. et al. 1999, A&A, 344, 857

George, I. M., & Fabian, A. C. 1991, MNRAS, 352, 369

Ghisellini, G., Haardt, F., & Matt, G. 1994, MNRAS, 267, 743

Heckman, T. M., Ptak, A., Hornschemeier, A., & Kauffmann, G. 2005, ApJ, 634, 161

Kikoin I. K. 1976, *Tables of Physical Quantities*, *Atomizdat*, *Moscow*

Levenson, N.A., Krolik, J.H., Zycki, P.T., Heckman, T.M., Weaver, K.A., Awaki, H., & Terashima, Y. 2002, ApJ, 573, L81

Lutz, D., Maiolino, R., Spoon, H. W. W., & Moorwood, F. M. 2004, A&A, 418, 465

Madau, P., Ghisellini, G., & Fabian, A.C. 1994, MNRAS, 270, 17

Magdziarz, P., & Zdziarski, A.A., 1995, MNRAS, 273, 837

Maiolino, R., Salvati, M., Dadina, M., Della Ceca, R., Matt, G., Risaliti, G., & Zamorani, G. 1998, A&A, 338, 781

Mitsuda, K. et al. 2007, PASJ, 59, S1

Mulchaey, J. S., Koratkar, A., Ward, M. J., Wilson, A. S., Whittle, M., Antonucci, R. J., Kinney, A. L., & Hurt, T. 1994, ApJ, 436, 586

Risaliti, G., Maiolono, R., & Salvati, M. 1999, ApJ, 522, 157

Ruiz, J.R., Crenshaw, D.M., Kraemer, S.B., Bower, G.A., Gull, T.R., Hutchings, J.B., Kaiser, M.E., & Weistrop, D. 2001, AJ, 122, 2961

Rybicki, G. B., & Lightman, A. P., 1979, *Radiative processes in Astrophysics*, Wilkey, New York.

Ueda, Y., Akiyama, M., Ohta, K., & Miyaji, T., 2003, ApJ, 598, 886

Verner, D.A., Ferland, G. J., Korista, K. T., & Yakovlev, D. G. 1996, ApJ, 465, 487

Wilman, R. J., & Fabian, A. C., 1999, MNRAS, 309, 862

Yaqoob, T., 1997, ApJ, 479, 184

This preprint was prepared with the AAS LaTeX macros v5.2.